Journal of Sound and Vibration 330 (2011) 5963–5981

Contents lists available at ScienceDirect

Journal of Sound and Vibration

journal homepage: www.elsevier.com/locate/jsvi

Identification of structural damage based on locally perturbed dynamic equilibrium with an application to beam component

Hao Xu [a], Li Cheng [a], Zhongqing Su [a,*], Jean-Louis Guyader [b]

[a] Department of Mechanical Engineering, The Hong Kong Polytechnic University, Kowloon, Hong Kong Special Administrative Region
[b] Laboratoire Vibrations Acoustique, Institut National des Sciences Appliquées (INSA) de Lyon, 69621 Villeurbanne, France

ARTICLE INFO

Article history:
Received 23 February 2011
Received in revised form
9 June 2011
Accepted 19 July 2011
Handling Editor: I. Trendafilova
Available online 15 August 2011

ABSTRACT

In recognition of the obvious limitations of most global vibration-based and local guided-wave-based damage detection techniques, a novel inverse identification approach was developed by canvassing the local perturbance to equilibrium characteristics of the structural component under inspection. Characterized by high-order spatial derivatives, this approach has in particular proven sensitivity to structural damage. Most importantly, it requires neither benchmark structures nor baseline signals; neither global models nor additional excitation sources as long as the structure undergoes steady vibration under its normal operation. Independent of a global model, prior knowledge on structural boundary conditions is not compulsory. To minimize unavoidable influence of measurement noise on high-order spatial derivatives, various de-noising treatments, including wavenumber filtering, optimal selection of measurement configuration and hybrid information fusion were introduced independently. Using a simple beam as a representative structural component for illustration, relationships among vibration frequency, density of measurement points and size of detectable damage were explored, facilitating a judicious selection of measurement parameters. Proof-of-concept validation was numerically conducted, and then experimentally demonstrated using a scanning laser vibrometer. In principle, this proposed methodology is applicable to a complex system comprising various structural components, provided that the local equilibrium relationships of the components are known *a priori*.
© 2011 Elsevier Ltd. All rights reserved.

1. Introduction

As a consequence of manufacturing defect, improper use, service wear, fatigue or even sabotage, engineering assets (*e.g.*, land/water/air/space vehicles, civil infrastructure and heavy equipment) experience continuous accumulation of damage over their lifespan. The damage, in whatever form it manifests, can considerably jeopardize the structural integrity and system functionality, potentially leading to catastrophic failure without timely detection. With safety being the paramount priority for all engineering assets, reliability, integrity and durability criteria must be strictly met. Towards this demanding requirement, a large variety of nondestructive evaluation (NDE) methods has been developed in the past, typified by radioscopy, ultrasonic inspection, shearography, magnetic resonance imagery, laser interferometry, acoustic emission, infrared thermography, eddy-current, *etc.* [1–7]. Most of these well-defined techniques can fulfill offline

* Corresponding author. Fax: +852 2365 4703.
E-mail address: MMSU@polyu.edu.hk (Z. Su).

0022-460X/$ - see front matter © 2011 Elsevier Ltd. All rights reserved.
doi:10.1016/j.jsv.2011.07.028

detection of local damage in small-scale structural fragments effectively. In practice, however, it is highly imperative to develop continuous and automated damage evaluation techniques conducive to online damage characterization. Such a consensus has entailed intensive research and development activities on structural health monitoring (SHM) in the past two decades.

In this aspect, majority of existing SHM techniques are either global vibration-based (using for example eigen-frequencies [8–10], mode shape or modal curvature [10,11], electro-mechanical impedance [12], flexibility matrix [13–15] and damping properties [16]) or local guided-wave-based (using for instance Lamb waves [17–24]). The basic rationale of global vibration-based detection resides on the fact that occurrence of damage induces changes in physical properties of a structure (*e.g.*, local stiffness, density, mass, thermal properties, electric/magnetic conductivity, and electro-mechanical impedance); and these changes are in turn manifested in dynamic responses captured from the structure. On the other hand, local guided-wave-based detection is based on wave scattering phenomena (*e.g.*, wave reflection, transmission, refraction and diffraction), mode conversion and energy absorption, upon interaction between the incident waves and damage existing in their propagation paths.

However, practical implementation of these vibration- or guided-wave-based detection techniques is somewhat hampered due to a number of obvious obstacles:

(i) a benchmark counterpart is often a prerequisite, from which baseline signals are obtained for comparison with signals acquired from the structure under inspection;
(ii) a pre-developed global model is vital to link changes in global responses or variations in local wave signals with damage parameters. The applicability and accuracy of a detection approach are substantially subject to the model;
(iii) approaches based on global vibration are excessively susceptible to structural boundary conditions; while most guided-wave-based methods require meticulous and strategic arrangements of sensor/actuators so as to avoid complex wave reflection from boundaries, leading to a very confined inspection region;
(iv) a well-controlled external excitation source is usually indispensible for activating structural vibration or guided waves, introducing additional complexity to the system and impeding realization of automated SHM; and
(v) last but not least, vibration-based methods, capitalizing on changes in global dynamic properties, are not sensitive to damage before it reaches a conspicuous extent, because damage is a local event which would not alter global responses phenomenally [25]. Guided-wave-based approaches can suffer from the wavelength of a selected wave mode, and, typically, only when the damage is larger than half the wavelength can it be detected [26].

Envisaging the above deficiencies of most existing global vibration-based and local guided-wave-based damage detection techniques, and driven by recent breakthroughs in advanced signal processing and measurement technology, a novel inverse damage identification technique was developed in this study, by canvassing locally perturbed dynamic equilibrium characteristics of a structural component governed by high-order spatial derivatives. The basic philosophy behind is that an intact structure locally satisfies a sort of dynamic equilibrium based on certain physical laws such as the local equation of motion. Upon occurrence of structural damage, the dynamic equilibrium is locally perturbed, and the perturbance in turn can be used as an indication of damage occurrence. Development of this approach was largely inspired by authors' previous work in reconstructing the distribution of excitation force applied on different structural elements [27,28]. In a sense, structural damage can likewise be regarded as an element creating perturbations as local excitation force to the structure within the damaged area. The proposed method requires NO benchmark structures, NO baseline signals, NO global structural model and therefore NO prior knowledge on structural boundary conditions, and NO additional excitation sources. In principle, it is applicable to a complex system comprising various structural components, provided that the local equilibrium relationship of the component of interest is known *a priori*. All these appealing features of the approach have ushered a new avenue to develop a practical SHM technique for complex systems in service.

The outline of the paper is as follows. Essence of the proposed methodology is illuminated in Section 2, focusing on establishing a damage index using a finite difference scheme. Proof-of-concept validation using finite element simulation is reported in Section 3. In this section, effect of measurement noise on accuracy and precision of the approach is quantified, which has motivated the introduction of wavenumber filtering for de-nosing. Dependence of detection accuracy on various measurement configurations (*e.g.*, vibration frequency and density of measurement points) is also discussed, with an aim to minimize noise influence on high-order derivatives. Taking advantages of the flexibility offered by the method, a data fusion scheme is in addition proposed to amalgamate various damage index plots. The proposed approach is then validated experimentally using a scanning laser vibrometer, detailed in Section 4.

2. Principle

Essence of this proposed approach can be stated in a straightforward way. Given a system comprising a variety of structural components, each identified component, in its intact status, satisfies a certain sort of structural equilibrium based on physical laws. In general, vibration of a structural component is governed by a set of equations of motion, which can be described in a general form as

$$[\mathbf{L}]\cdot[\mathbf{u}] = [\mathbf{F}]\cdot\delta(M-M_e), \tag{1}$$

where [**L**] is a matrix differential operator, [**u**] the structural displacement, and [**F**] the external excitation force applied on the surface of the component at location M_e; δ is a Dirac function which vanishes at M when $M \neq M_e$. In the case that the component has a free surface, and is not subject to any direct excitation other than those internal forces/moments exerted by its adjacent components through their sharing boundaries (*i.e.*, $M \neq M_e$), Eq. (1) becomes

$$[\mathbf{L}] \cdot [\mathbf{u}] = 0. \tag{2}$$

Note that Eq. (2) applies to every single point or element of the discussed structural component, serving as therefore a local equilibrium equation and reflecting the local equilibrium correlation between the inertia force of a structural element and the internal forces/moments exerted by its adjacent elements. In this sense, even in the absence of any external force, Eq. (2) is still able to describe the forced vibration of a structural element (excitation is exerted by its adjacent elements). Provided [**u**] can be obtained through measurement, any drastic deviation from zero in the left-hand-side term of Eq. (2) at a particular spatial position of the component implies, in principle, local breakage of the structural equilibrium, *i.e.*, occurrence of damage therein.

The left-hand-side term of Eq. (2) is defined as a *damage index* (DI) hereinafter. Before proceeding to technical details, it is worthy of highlighting the appealing features of damage detection based on the above philosophy:

(i) because the proposed method locally examines individual parts of an assembly, independently of rest of the whole system, a global model is not required. By the same token, the complexity of the system such as boundary conditions would not limit the applicability of the approach, provided that the local equilibrium characteristics of a structural component of current interest are known;
(ii) for the same sake, no benchmark structure or baseline signal is required *a priori*;
(iii) knowledge on structural boundary condition is not required beforehand;
(iv) as long as the structural component undergoes steady vibration (*e.g.*, under the normal operation of the system), no additional excitation source is compulsory, which provides great flexibility to automated SHM applications.

In theory this method is applicable to a complex system comprising various structural components such as beams, plates and shells, regardless of the type and number, provided that local equilibrium relationship for the component of interest is available. Taking a homogeneous and isotropic Euler-Bernoulli beam component subjected to a flexural (transverse) excitation as a simple example for illustration, DI in Eq. (2) can be condensed to a single transverse component as a result of de-coupling between the in-plane motion and out-of-plane motion. In a harmonic regime, it has

$$\mathrm{DI} = EI\frac{\mathrm{d}^4 w(x)}{\mathrm{d}x^4} - \rho S\omega^2 w(x), \tag{3}$$

where $w(x)$ is the transverse displacement of the beam at x; E, ρ, I and S are the complex Young's modulus (including material damping), density, moment of inertia and cross-section area of the beam, respectively; ω is the angular frequency of the vibration (in general, ω is determined by the 'natural excitation' of the structural component under its normal operation). In the case that the natural excitation is not harmonic, a frequency component in the frequency domain after Fourier transform can also be used. Appropriate selection of ω is to be discussed in subsequent sections. It is relevant to note that the system damping is apprehended in complex modulus E. In practice, however, estimate of damping is tedious and its effects can become pronounced only in the vicinity of the resonance region. Therefore, it is preferable to apply this method at off-resonance regime of the structure under inspection, so as to minimize the effect of system damping. The proposed method provides such flexibility in frequency selection, to be demonstrated later in this paper.

With occurrence of damage, anticipated changes in DI can be illustrated using the above beam component. Assume that (i) this beam component bears a crack of a certain length ($X_1 < x < X_2$) along the beam span as schematically shown in Fig. 1; and (ii) the damage can be represented by $\Delta_{\rho S}$ and Δ_{EI}, where $\Delta_{\rho S}$ and Δ_{EI} are multiplicative reductions in mass and stiffness in the damaged zone compared with its intact status, respectively. Thus, it has, in Fig. 1

in the intact zones ($x < X_1$ or $x > X_2$):

$$\mathrm{DI} = EI\frac{\mathrm{d}^4 w(x)}{\mathrm{d}x^4} - \rho S\omega^2 w(x) = 0; \tag{4}$$

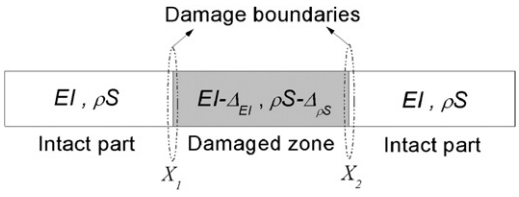

Fig. 1. Schematic of a beam component bearing a damaged zone.

within the damaged zone ($X_1 \le x \le X_2$):

$$\mathrm{DI} = EI\frac{\mathrm{d}^4w(x)}{\mathrm{d}x^4} - \rho S\omega^2 w(x) = \left[(EI-\Delta_{EI})\frac{\mathrm{d}^4w(x)}{\mathrm{d}x^4} - (\rho S-\Delta_{\rho S})\omega^2 w(x)\right] + \left[\Delta_{EI}\frac{\mathrm{d}^4w(x)}{\mathrm{d}x^4} - \Delta_{\rho S}\omega^2 w(x)\right] = \left[\Delta_{EI}\frac{\mathrm{d}^4w(x)}{\mathrm{d}x^4} - \Delta_{\rho S}\omega^2 w(x)\right]. \tag{5}$$

Treatment of boundaries of the damaged zone requires more meticulous handling, as detailed as follows. The continuity conditions at the left boundary of the damaged zone ($x=X_1$), can be stated as

Flexural displacement:

$$\lim_{\varepsilon\to 0}\{w(X_1-\varepsilon)\} = \lim_{\varepsilon\to 0}\{w(X_1+\varepsilon)\}; \tag{6a}$$

Slope:

$$\lim_{\varepsilon\to 0}\left\{\frac{\mathrm{d}w(X_1-\varepsilon)}{\mathrm{d}x}\right\} = \lim_{\varepsilon\to 0}\left\{\frac{\mathrm{d}w(X_l+\varepsilon)}{\mathrm{d}x}\right\}; \tag{6b}$$

Bending moment:

$$\lim_{\varepsilon\to 0}\left\{EI\frac{\mathrm{d}^2w(X_1-\varepsilon)}{\mathrm{d}x^2}\right\} = \lim_{\varepsilon\to 0}\left\{(EI-\Delta_{EI})\frac{\mathrm{d}^2w(X_1+\varepsilon)}{\mathrm{d}x^2}\right\} = M(X_1); \tag{6c}$$

Shear force:

$$\lim_{\varepsilon\to 0}\left\{EI\frac{\mathrm{d}^3w(X_1-\varepsilon)}{\mathrm{d}x_3}\right\} = \lim_{\varepsilon\to 0}\left\{(EI-\Delta_{EI})\frac{\mathrm{d}^3w(X_1+\varepsilon)}{\mathrm{d}x^3}\right\} = T(X_1); \tag{6d}$$

where $T(X_1)$ and $M(X_1)$ are the internal shear force and bending moment of the beam at X_1, respectively. Eqs. (6c) and (6d) can be re-arranged as, respectively

$$\lim_{\varepsilon\to 0}\left\{\frac{\mathrm{d}^2w(X_1+\varepsilon)}{\mathrm{d}x^2} - \frac{\mathrm{d}^2w(X_1-\varepsilon)}{\mathrm{d}x^2}\right\} = \left(\frac{1}{(EI-\Delta_{EI})} - \frac{1}{EI}\right)M(X_1); \tag{6e}$$

and

$$\lim_{\varepsilon\to 0}\left\{\frac{\mathrm{d}^3w(X_1+\varepsilon)}{\mathrm{d}x^3} - \frac{\mathrm{d}^3w(X_1-\varepsilon)}{\mathrm{d}x^3}\right\} = \left(\frac{1}{(EI-\Delta_{EI})} - \frac{1}{EI}\right)T(X_1). \tag{6f}$$

It can be seen that the second and third-order derivatives of the flexural displacement of the beam, $w(x)$, are discontinuous across the boundary of the damaged zone (at $x=X_1$).

Similarly, at the other boundary of the damaged zone (at $x=X_2$), it has

$$\lim_{\varepsilon\to 0}\left\{\frac{\mathrm{d}^2w(X_2+\varepsilon)}{\mathrm{d}x^2} - \frac{\mathrm{d}^2w(X_2-\varepsilon)}{\mathrm{d}x^2}\right\} = -\left(\frac{1}{(EI-\Delta_{EI})} - \frac{1}{EI}\right)M(X_2), \tag{7a}$$

and

$$\lim_{\varepsilon\to 0}\left\{\frac{\mathrm{d}^3w(X_2+\varepsilon)}{\mathrm{d}x^3} - \frac{\mathrm{d}^3w(X_2-\varepsilon)}{\mathrm{d}x^3}\right\} = -\left(\frac{1}{(EI-\Delta_{EI})} - \frac{1}{EI}\right)T(X_2). \tag{7b}$$

Eq. (6e) can be used to calculate $EI(\mathrm{d}^3w/\mathrm{d}x^3)$ as follows (at $x=X_1$):

$$\begin{aligned} EI\frac{\mathrm{d}^3w(x)}{\mathrm{d}x^3} &= E\lim_{\varepsilon\to 0}\left\langle\left\{\frac{\mathrm{d}^2w(X_1+\varepsilon)}{\mathrm{d}x^2} - \frac{\mathrm{d}^2w(X_1-\varepsilon)}{\mathrm{d}x^2}\right\}/2\varepsilon\right\rangle = EI\left(\frac{1}{(EI-\Delta_{EI})} - \frac{1}{EI}\right)M(X_1)\lim_{\varepsilon\to 0}\left(\frac{1}{2\varepsilon}\right) \\ &= \frac{1}{2}\left(\frac{EI}{(EI-\Delta_{EI})} - 1\right)M(X_1)\delta(x-X_1). \end{aligned} \tag{8}$$

Eq. (8) can further be employed to obtain $EI(\mathrm{d}^4w/\mathrm{d}x^4)$ (at $x=X_1$):

$$\begin{aligned} EI\frac{\mathrm{d}^4w}{\mathrm{d}x^4} &= \frac{1}{2}\left(\frac{EI}{(EI-\Delta_{EI})} - 1\right)\left\{\frac{\mathrm{d}M(X_1)}{\mathrm{d}x}\delta(x-X_1) + M(X_1)\delta'(x-X_1)\right\} \\ &= \frac{1}{2}\left(\frac{EI}{(EI-\Delta_{EI})} - 1\right)\{T(X_1)\delta(x-X_1) + M(X_1)\delta'(x-X_1)\}. \end{aligned} \tag{9}$$

In Eq. (9), $\delta'(x)$ is the first-order derivative of Dirac functionn $\delta(x)$. Similar derivation also applies to the other boundary of the damaged zone ($x=X_2$).

Combining Eqs. (4), (5) and (9), the following general expression, valid across the whole beam span, can be obtained

$$\begin{aligned}\mathrm{DI} = EI\frac{\mathrm{d}^4w(x)}{\mathrm{d}x^4} - \rho S\omega^2 w(x) = \left(\Delta_{EI}\frac{\mathrm{d}^4w(x)}{\mathrm{d}x^4} - \Delta_{\rho S}\omega^2 w(x)\right)(H(x-X_1)-H(x-X_2))\\ +\frac{1}{2}\left(\frac{EI}{(EI-\Delta_{EI})}-1\right)T(X_1)\delta(x-X_1)+\frac{1}{2}\left(\frac{EI}{(EI-\Delta_{EI})}-1\right)M(X_1)\delta'(x-X_1)\\ -\frac{1}{2}\left(\frac{EI}{(EI-\Delta_{EI})}-1\right)T(X_2)\delta(x-X_2)-\frac{1}{2}\left(\frac{EI}{(EI-\Delta_{EI})}-1\right)M(X_2)\delta'(x-X_2),\end{aligned} \tag{10}$$

where $H(x)$ is a Heaviside function.

Eq. (10) indicates that DI equals to zero in the intact region; within the damaged zone, DI varies smoothly as calibrated by the first right-hand-side residual term in Eq. (10). Drastic deviation of DI from zero is anticipated at the damage boundaries where the Dirac function ($\delta(x)$) and its derivatives ($\delta'(x)$) change significantly. Therefore, it is expected that this method is highly sensitive to damage boundaries in terms of the drastic perturbance to DI at boundaries.

The flexural displacement of the beam component under steady vibration can be discretely acquired using a number of well-defined measurement techniques and devices such as accelerometers, laser holography or Doppler laser vibrometer, whereby the high-order derivatives in Eq. (10) at a discrete measurement point i can be obtained using a finite difference scheme in the light of its neighboring measurement points closely spaced. In a discrete form, the damage index at measurement point i, DI_i, is, if four neighboring measurement points from point $i-2$ to $i+2$ are involved,

$$\mathrm{DI}_i = \frac{EI}{D_m^4}(w_{i+2}-4w_{i+1}+6w_i-4w_{i-1}+w_{i-2})-\rho S\omega^2 w_i, \tag{11}$$

where w_i is the flexural displacement measured at point i. In Eq. (11), D_m is the interval between two adjacent measurement points.

It is noteworthy that, not only the above-detailed detection philosophy is applicable to a structural beam, but also can it be used to other structural components with known local equilibrium (*e.g.*, a plate or a shell). For example, for a plate-like component, without the necessity of concerning the complexity of its boundary conditions and geometric shapes (these factors are crucial in conventional global vibration-based detection), DI can be constructed in a similar way using the local equilibrium for the plate element, as

$$\mathrm{DI} = \frac{Eh^3}{12(1-\nu^2)}\left(\frac{\partial^4w(x,y)}{\partial x^4}+\frac{\partial^4w(x,y)}{\partial y^4}+2\frac{\partial^4w(x,y)}{\partial^2x\partial^2y}\right)-\rho h\omega^2 w(x,y), \tag{12}$$

where E, ρ, h and ν are complex Young's modulus, density, thickness and Poisson's ratio of the plate, respectively. $w(x,y)$ is the transverse displacement of the plate at (x,y). Likewise, Eq. (12) can be discretized at measurement point (i,j) using a finite difference scheme as

$$\mathrm{DI}_{i,j} = \frac{Eh^3}{12(1-\nu^2)}(\chi_{i,j}^{4x}+\chi_{i,j}^{4y}+2\chi_{i,j}^{2x2y})-\rho h\omega^2 w_{i,j}, \tag{13}$$

where $w_{i,j}$ is the flexural displacement of the plate measured at point (i,j), and

$$\begin{aligned}\chi_{i,j}^{4x} &= \frac{\partial^4 w}{\partial x^4} = \frac{1}{\Delta_x^4}(w_{i+2,j}-4w_{i+1,j}+6w_{i,j}-4w_{i-1,j}+w_{i-2,j}),\\ \chi_{i,j}^{4y} &= \frac{\partial^4 w}{\partial y^4} = \frac{1}{\Delta_y^4}(w_{i,j+2}-4w_{i,j+1}+6w_{i,j}-4w_{i,j-1}+w_{i,j-2}),\\ \chi_{i,j}^{2x2y} &= \frac{\partial^4 w}{\partial^2 x\partial^2 y} = \frac{1}{\Delta_x^2\Delta_y^2}(w_{i+1,j+1}-2w_{i+1,j}+w_{i+1,j-1}-2w_{i,j+1}+4w_{i,j}-2w_{i,j-1}+w_{i-1,j+1}-2w_{i-1,j}+w_{i-1,j-1}),\end{aligned} \tag{14}$$

if twelve neighboring measurement points are involved for the finite difference.

3. Proof-of-concept validation using numerical simulation

Proof-of-concept validation for the proposed damage detection approach was carried out using finite element (FE) simulation. Without loss of generality, a homogeneous and isotropic Euler-Bernoulli beam was used as a simple example.

3.1. In the absence of measurement noise

Consider a cantilever beam (1440 mm long, 20 mm wide and 20 mm thick; Young's Modulus: $200\times(1+10^{-4}i)$ GPa; density: 7800 kg/m^3), clamped at its left end and bearing a through-width damaged zone from $x_d+d/2$ to $x_d-d/2$ along the beam axis (centralized at x_d with a length of d), as shown in Fig. 2. The whole beam was modeled with a total of 144 beam elements (10 mm in length for each element). The damage was simulated with a reduction in Young's modulus of corresponding elements within the damaged zone by 30% of their original value. The beam was excited by a harmonic

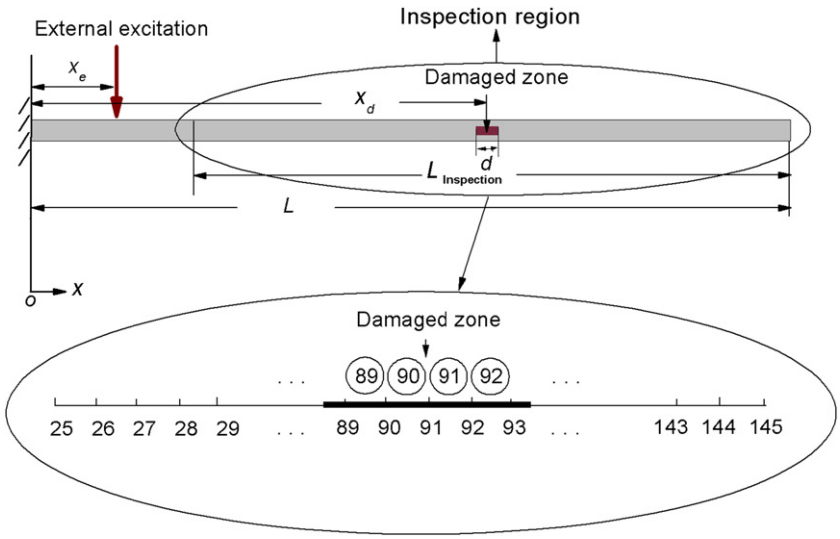

Fig. 2. FE model of a cantilever beam bearing a damaged zone for proof-of-concept validation.

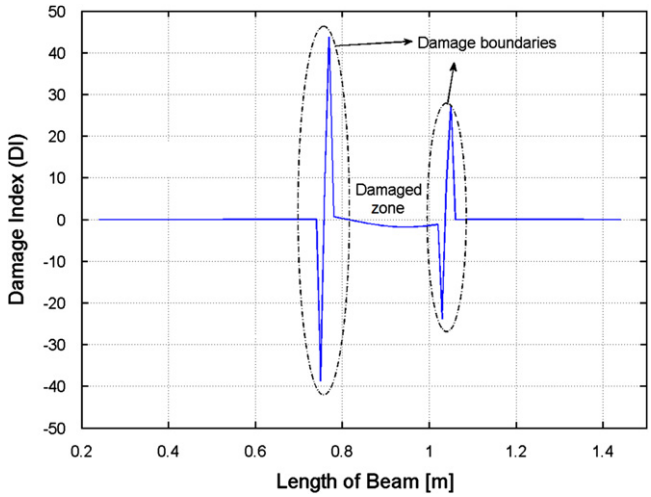

Fig. 3. Constructed DI_i throughout inspection region for the beam in Fig. 2 (x_d=900 mm and d=280 mm).

point force of frequency f at x_e=120 mm, as indicated in Fig. 2. To avoid any singularity near the excitation force, an inspection region ($L_{\text{Inspection}}$) was selected by excluding the vicinity of x_e. The flexural displacements at all FE nodes (corresponding to those measurement points in subsequent experiment) were obtained using ANSYS®, to construct DI_i in terms of Eq. (11). Fig. 3 exemplarily shows the calculated DI_i across the inspection region ($L_{\text{Inspection}}$=1200 mm, meshed by 120 elements) when x_d=900 mm, d=280 mm and f=550 Hz. In the figure, distribution of DI_i calculated from simulation coincides with the prediction using Eq. (10): DI_i remains zero in intact regions and deviates from zero in damaged zone, with prominent Dirac changes at two boundaries of the damaged zone. Note that the spikes at the damage boundaries are not symmetrical with respect to DI_i=0, because of the asymmetrical Dirac function component.

Further, reducing length of the damaged zone from d=280 mm to d=20 mm (x_d=900 mm), the calculated DI_i across the inspection region is displayed in Fig. 4(a) against the beam span. Though Dirac oscillation of DI_i at two boundaries of the damaged zone overlaps as a result of the reduced d (this might pose certain difficulty in explicitly differentiating individual damage boundaries), overall size of the damaged zone is still distinguishable, more clearly seen in Fig. 4(b) which presents the absolute value of DI_i only.

3.2. *In the presence of measurement noise*

In practical implementation, measurement noise is unavoidable. Such noise interference can be exacerbated for this proposed approach because measurement noise can considerably contaminate high-order derivatives of displacement in

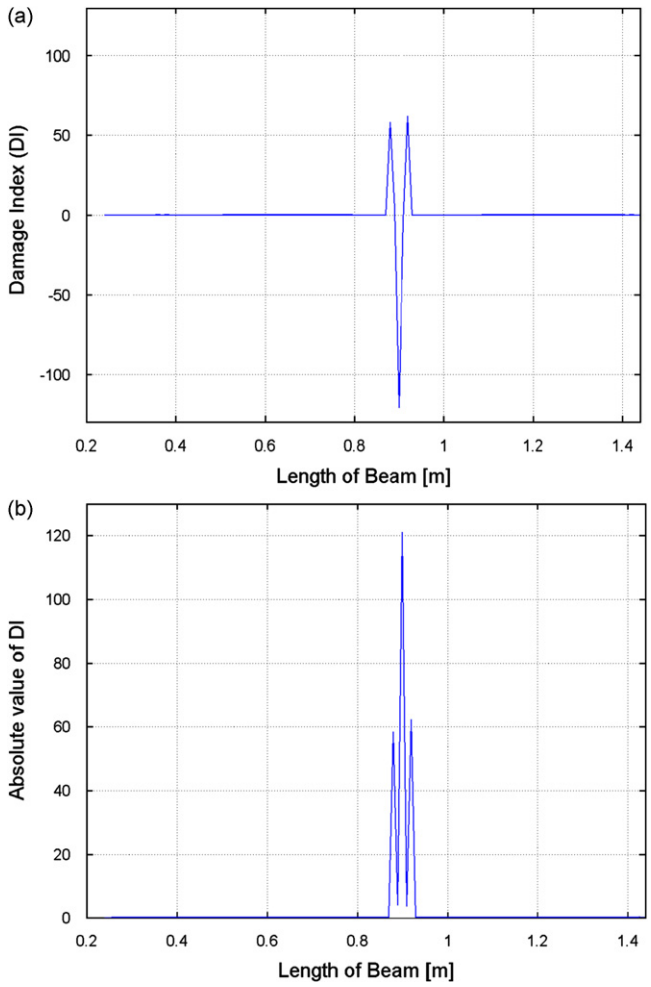

Fig. 4. (a) Constructed DI_i throughout inspection region for the beam in Fig. 2 (x_d=900 mm and d=20 mm) and (b) absolute value of DI_i in (a).

the constructed DI_i, masking information pertaining to the damage. To quantitatively examine tolerance of the developed approach to measurement noise, a certain amount of noise disturbance was added to the calculated displacements at FE nodes in accordance with

$$w_i^{\text{noisy}} = w_i^{\text{exact}} \Delta w e^{j\Delta\varphi}, \tag{15}$$

where w_i^{exact} and w_i^{noisy} are the noise-free displacement obtained at measurement point i from simulation and its corresponding noise-polluted counterpart; Δw is a Gaussian random real number related to the magnitude of w_i^{exact}; $\Delta\varphi$ is an another Gaussian random real number related to phase of w_i^{exact}. Fig. 5(a) shows the respectively constructed DI_i using w_i^{exact} and w_i^{noisy} (in the latter, the mean of Δw is one with a standard deviation being 1% of the magnitude, whilst the mean of $\Delta\varphi$ is zero with a standard deviation being 1° of the phase). With noise pollution (dashed line in Fig. 5(a)), constructed DI_i does not offer any information for damage localization, calling for appropriate de-noising treatment.

3.3. De-noising through low-pass wavenumber filtering

Prior to de-noising, spectrographic analysis was applied to canvass calculated DI_i in a wavenumber domain. Using the two DI_i curves in Fig. 5(a) (with and without added noise) for illustration, distributions of DI_i for these two cases in the wavenumber domain upon Fourier transform are shown in Fig. 5(b), showing certain overlapping in between at lower wavenumbers and dominance of noise at higher wavenumbers. By observing this, a low-pass filter was designed, defined in the wavenumber domain as

$$\begin{aligned} \tilde{h}(k) &= 1 \quad (k \in [-k_c, +k_c]), \\ \tilde{h}(k) &= 0 \quad (k \in [-\infty, -k_c] \cup [+k_c, +\infty]), \end{aligned} \tag{16}$$

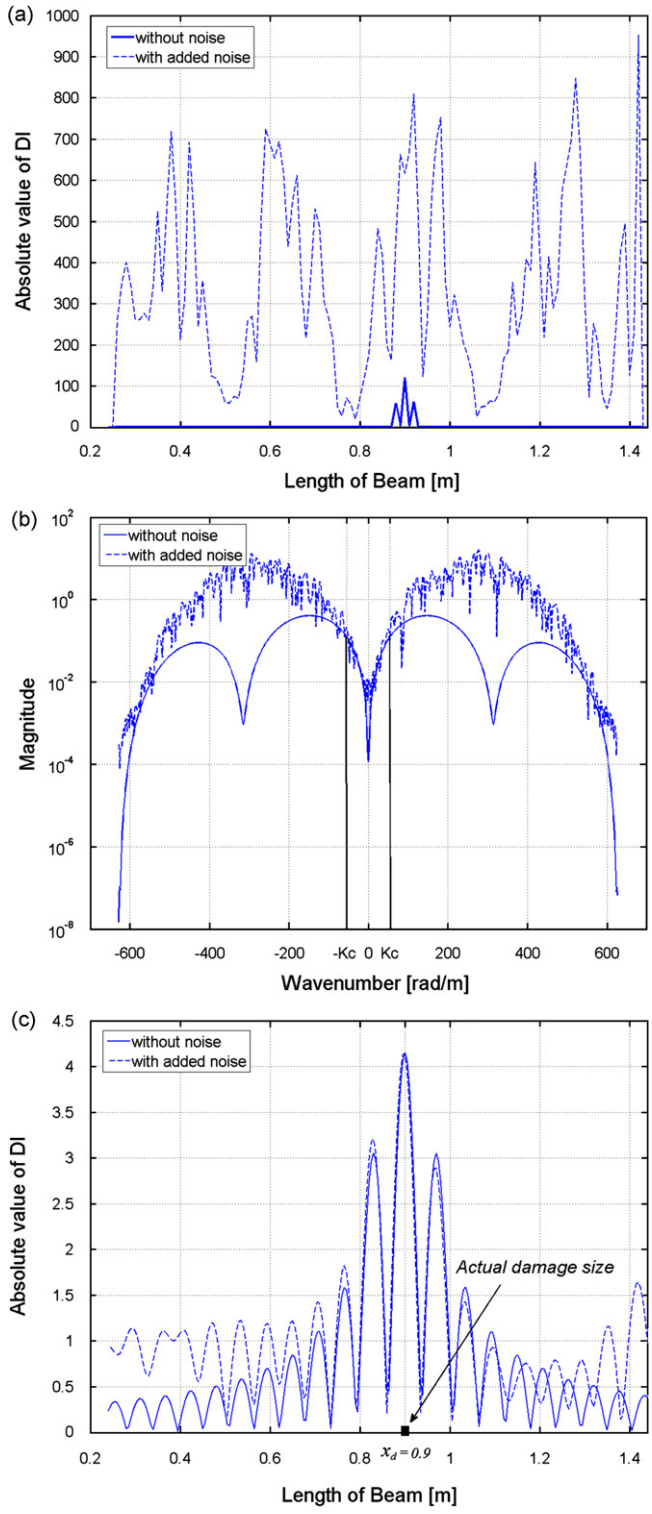

Fig. 5. Constructed DI_i using noise-free nodal displacements (solid line) and noise-contaminated nodal displacements (dashed line) for the beam in Fig. 2: (a) in spatial domain; (b) in wavenumber domain; and (c) re-constructed DI_i upon application of low-pass wavenumber filtering (k_c=55 rad/m).

where k is the wavenumber; $\tilde{h}(k)$ the transfer function of an ideal filter in the wavenumber domain; k_c the cutoff wavenumber with a unit of rad $\times$ m^{-1}, as indicated in Fig. 5(b). In addition, in order to minimize the influence from boundaries of the inspection region (known as the *Gibbs phenomenon* [28]), a rectangular window, $\Psi(x)$, was

multiplicatively applied to the calculated DI_i prior to the above wavenumber filtering. The window was defined as

$$\Psi(x)=0.5\left(1-\cos\frac{\pi x}{\alpha}\right) \quad (x<\alpha),$$
$$\Psi(x)=1 \quad (\alpha\le x\le L_{\text{Inspection}}-\alpha),$$
$$\Psi(x)=0.5\times\left(1-\cos\frac{\pi(x-L_{\text{Inspection}}+2\alpha)}{\alpha}\right) \quad (x>L_{\text{Inspection}}-\alpha), \tag{17}$$

where $\alpha=2\pi/k_c$. Upon application of the rectangular window and wavenumber filtering, Fig. 5(c) shows the re-constructed DI_i for the two signals in Fig. 5(a) (when $k_c=55$ rad/m), able to highlight the location and size of the damaged zone roughly.

3.4. De-noising through proper selection of measurement parameters

Characterized by high-order spatial derivatives ($d^4w(x)/dx^4$)), it is anticipated that accuracy of the approach is somewhat subject to a variety of factors during measurement of $w(x)$.

3.4.1. Damage location vs. distribution of internal bending moment

Subjected to an external excitation, the structural component manifests various vibration patterns. Under different patterns, sensitivity of the method varies. To explore such an issue, up to 59 damage scenarios were considered in the simulation, in each of which the discussed beam component bore a damaged zone of the same length ($d=20$ mm) at different locations ($x_d=260$–1420 mm, with an increment of 20 mm within the inspection region $L_{\text{Inspection}}=1200$ mm). A transverse excitation ($x_e=120$ mm, $f=550$ Hz) was applied, under which DI_i was calculated at each measurement point and the maximum absolute value of DI_i, $|DI_i|_{\max}$, for each scenario was extracted. Fig. 6 presents variation in $|DI_i|_{\max}$ for the 59 damage scenarios and distribution of internal bending moment of the intact beam under the same excitation, to notice a consistence in between. This observation implies that, when the damage is right located at or near the position at which the internal bending moments is relatively large, the local breakage of equilibrium can be more pronouncedly reflected (a larger DI_i), benefiting the detection exercise.

3.4.2. Density of measurement points vs. vibration frequency

Allowing for the fact that accuracy of the finite difference calculation can be slaved to the number of measurement points involved, different densities of measurement points in $L_{\text{Inspection}}$ were comparatively used to construct DI_i. Let D_m be the interval between two adjacent measurement points and λ be the wavelength of the vibration of the beam at a given excitation frequency, Fig. 7 shows distributions of DI_i for the discussed beam calculated using nodal displacements at different ratios of D_m/λ ($D_m/\lambda=0.017$, 0.033, 0.050, 0.067, 0.100, 0.133), without and with added noise (noise was added using Eq. (15) as detailed in Section 3.2). It can be seen that, with the increase of D_m/λ (from (a) to (f)), (i) DI_i in the absence of noise (solid lines) gradually loses its capacity of depicting the location and size of the damaged zone, whereas (ii) DI_i in the absence of noise (solid lines) coincides more with DI_i in the presence of noise (dashed lines), indicating an increasing similarity between noise-polluted and noise-free signals. These two observations suggest a dual-effect of D_m/λ: using less measurement points at a given excitation frequency (greater D_m/λ) enhances the noise immunity of the approach, while this scarifies the accuracy of finite difference, and *vice versa*.

Therefore, a judicious selection of D_m/λ is critical to strike a balance between accuracy of the method and its capacity of noise immunity. To quantify this dual-effect, two normalized signal parameters, AD (representing Accuracy of finite Difference) and NI (representing Noise Influence), were introduced for following discussion.

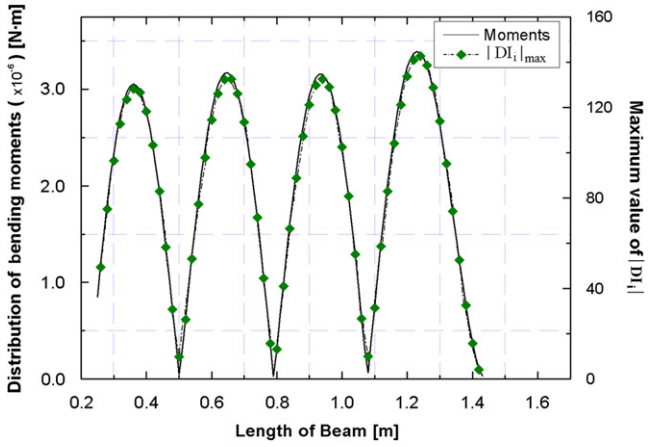

Fig. 6. Comparison between $|DI_i|_{\max}$ for 59 damage scenarios and internal bending moment of the intact beam ($f=550$ Hz).

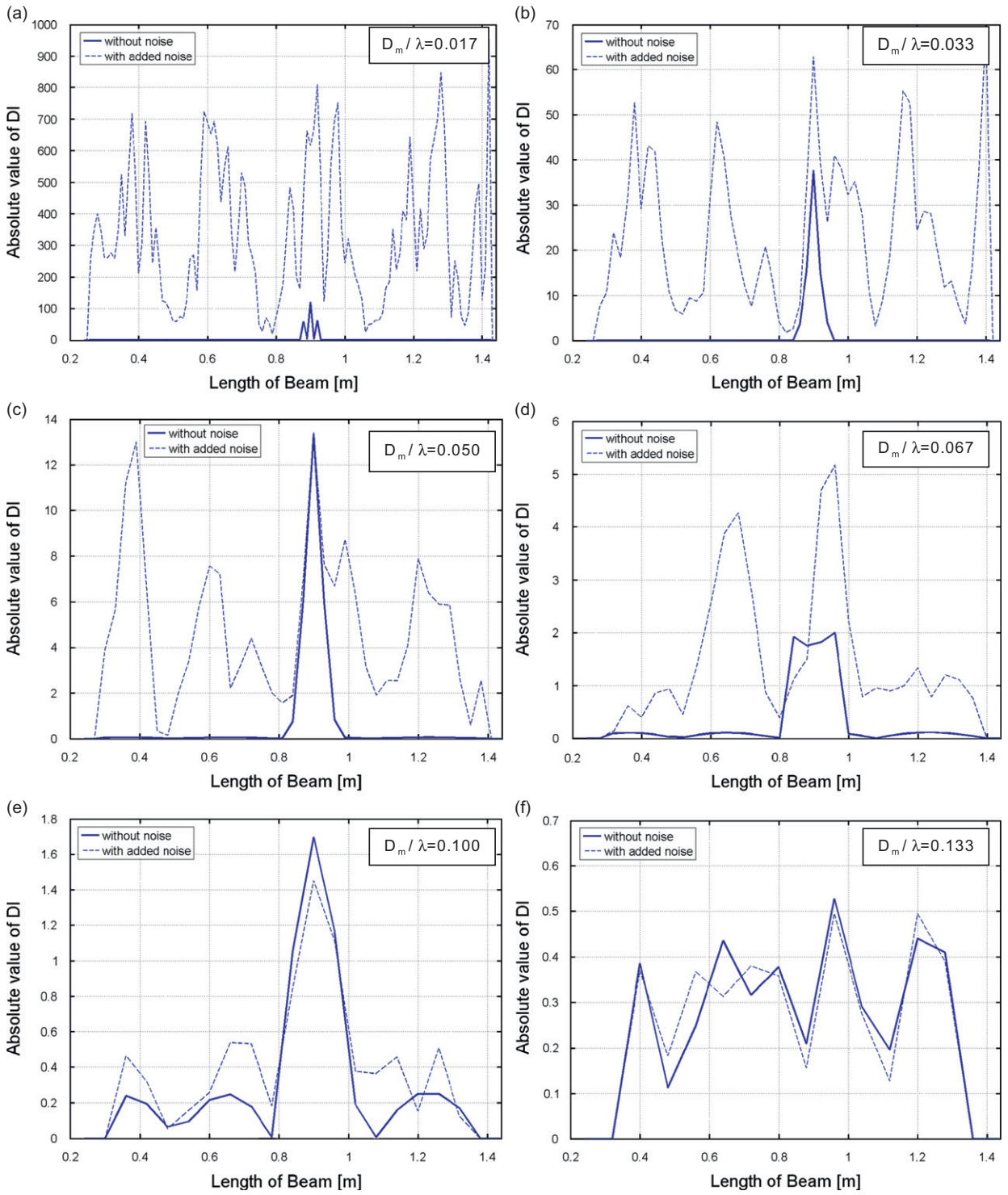

Fig. 7. Constructed DI_i using noise-free nodal displacements (solid line) and noise-contaminated nodal displacements (dashed line) for the beam in Fig. 2 when D_m/λ is (a) 0.017; (b) 0.033; (c) 0.050; (d) 0.067; (e) 0.100; and (f) 0.133.

3.4.2.1. AD. Using the above-discussed beam for illustration, an *effective damaged zone* was first defined, centralized at x_d and containing the peak values of DI_i as a result of Dirac changes near damage boundaries, as shown in Fig. 8(a). Obviously length of the effective damaged zone is associated with D_m, and it is in principle larger than the actual length of the

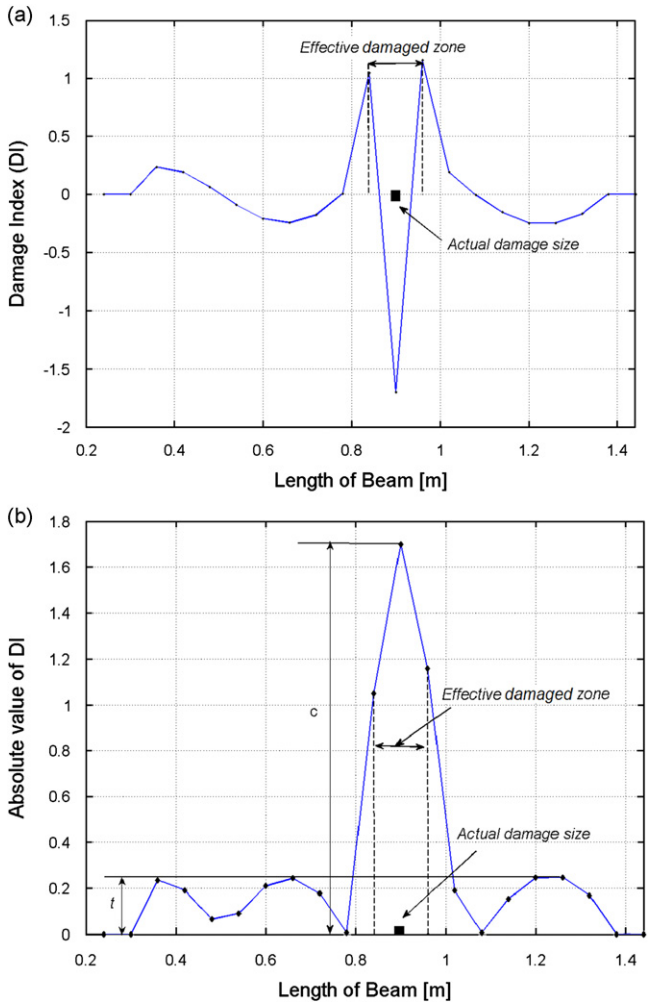

Fig. 8. Definition of (a) effective damaged zone and (b) signal parameter AD.

damaged zone because the construction of DI_i using the finite difference at damage boundaries involves neighboring measurement points beyond the damaged zone. Letting the maximum peak value of DI_i within the effective damaged zone be c, the maximum peak value of DI_i outside the effective zone (but within $L_{\text{Inspection}}$) be t (highlighted in Fig. 8(b)) and the mean of all DI_i throughout $L_{\text{Inspection}}$ be a, AD is then defined as

$$\text{AD} = \frac{t}{a}. \tag{18a}$$

The incentive of establishing the above AD is to introduce a normalized parameter, able to quantify the accuracy of finite difference. The underlying hypostasis of AD can be better understood by re-arranging it as

$$\text{AD} = \frac{t}{a} = \frac{t/c}{a/c}, \tag{18b}$$

in which the numerator represents the relative fluctuation of DI_i in the intact zone (due to noise) with regard to the maximum changes in the signal due to presence of damage (c), and it additionally shows the relative dominance of the damage-induced changes in DI_i. In particular, the smaller the ratio t/c, the more prominent is DI_i in the effective damaged zone. On the other hand, the denominator reflects the mean of all damage indices (due to both damage and noise) with regard to the maximum changes in the signal due to presence of damage (c). Accuracy of the finite difference is deemed acceptable when $0 < \text{AD} \leq 1$ (for example, those signals in Fig. 7(a)–(e), in which both location and size of the damaged zone can be captured roughly without applying any de-noising treatment such as the low-pass wavenumber filtering aforementioned); while the approach presents low accuracy when $\text{AD} > 1$ (for example, the signal in Fig. 7(f)), failing to describe the damage without applying any de-noising treatment.

3.4.2.2. NI. Along the same line of consideration for developing AD, the index, NI, is defined as

$$\mathrm{NI} = \frac{1-\Xi}{1-\Xi_c}, \tag{19a}$$

where Ξ is the correlation coefficient between two DI_i curves in the absence (ideal case) and presence of measurement noise (practical case). The correlation coefficient is given by

$$\Xi = \frac{N\sum_{i=1}^{N}\mathrm{DI}_i^{\mathrm{noisy}}\mathrm{DI}_i^{\mathrm{exact}} - \sum_{i=1}^{N}\mathrm{DI}_i^{\mathrm{noisy}}\sum_{i=1}^{N}\mathrm{DI}_i^{\mathrm{exact}}}{\sqrt{N\sum_{i=1}^{N}(\mathrm{DI}_i^{\mathrm{noisy}})^2-\left(\sum_{i=1}^{N}\mathrm{DI}_i^{\mathrm{noisy}}\right)^2}\sqrt{N\sum_{i=1}^{N}(\mathrm{DI}_i^{\mathrm{exact}})^2-\left(\sum_{i=1}^{N}\mathrm{DI}_i^{\mathrm{exact}}\right)^2}}, \tag{19b}$$

where $\mathrm{DI}_i^{\mathrm{noisy}}$ and $\mathrm{DI}_i^{\mathrm{exact}}$ stand for the damage indices calculated using nodal displacements with and without added noise, respectively. N is the number of measurement points in $L_{\mathrm{Inspection}}$. The greater the similarity between $\mathrm{DI}_i^{\mathrm{noisy}}$ and $\mathrm{DI}_i^{\mathrm{exact}}$, the closer to unity is the coefficient Ξ. In Eq. (19a), Ξ_c is a threshold, over which the measurement noise influence is deemed significant leading to poor recognizability of signals. When $0<\mathrm{NI}\le 1$ (*i.e.*, $\Xi \ge \Xi_c$), $\mathrm{DI}_i^{\mathrm{noisy}}$ and $\mathrm{DI}_i^{\mathrm{exact}}$ exhibit high coincidence (for example, those signals in Fig. 7(e) and (f)), indicating that measurement noise become negligible; while when $\mathrm{NI}>1$ (*i.e.*, $\Xi<\Xi_c$), deviates significantly from $\mathrm{DI}_i^{\mathrm{exact}}$ (for example, those signals in Fig. 7(a)–(d)), making damage identification impossible if without any de-noising treatment.

From the above twofold discussion, it becomes clear that an ideal scenario is the case in which both AD and NI are as low as possible, or at least below the unity. In order to determine an optimal D_m/λ so as to ensure both AD and NI are in acceptable levels, signals shown in Fig. 7 were further processed to extract their corresponding AD and NI values. Fig. 9 displays the variations in AD and NI at different selections of D_m/λ. The ascending trend for AD and descending trend for NI with an increase in D_m/λ reconfirm previous observation and analysis. Most importantly, when D_m/λ is around 0.1, both AD and NI fall into acceptable levels ($0<\mathrm{AD}\le 1$ and $0<\mathrm{NI}\le 1$). Such a selection of $D_m/\lambda=0.1$ corresponds to the case shown in Fig. 7(e) where roughly TEN measurement points per wavelength were used for constructing DI_i, reaching a compromise between signal recognizability and tolerance to measurement noise. In Fig. 7(e), damage can be estimated roughly even without application of any de-nosing treatment such as the low-pass wavenumber filtering.

To better show the dependence of both parameters on D_m/λ, AD and NI are plotted in a two-dimensional presentation (AD–NI), in Fig. 10, for those signals in Fig. 7. According to the above-addressed criterion, selection of AD and NI in the shadowed region ($0<\mathrm{AD}\le 1$ and $0<\mathrm{NI}\le 1$) is deemed optimal to deliver satisfactory identification results without relying on any signal de-nosing treatment. Using an optimal D_m/λ, accuracy of the finite difference can be guaranteed and at the same time the noise interference is negligible, so that the location of damage can be directly identified without using the wavenumber-based filtering. It is noteworthy that an optimal selection of D_m/λ is obviously dependent on the noise level. Should the measurement noise level be lower, NI becomes less important in determining D_m/λ. Under such a circumstance more measurement point should be used to enhance the identification accuracy.

3.4.3. Damage extent vs. AD and NI

As envisaged, precision of the proposed detection approach can also be affected by either size of the damaged zone relative to the wavelength of vibration (*i.e.*, d/λ) or severity of the damage (degree of stiffness reduction, denoted by SR in what follows), apart from D_m/λ as discussed previously.

For discussion, keeping the same forced excitation (*i.e.*, the same λ) but changing length of the damaged zone (d), various ratios of d/λ were obtained. Fig. 11 exemplarily shows six cases when $d/\lambda=0.017$, 0.033, 0.067, 0.100, 0.133, 0.167,

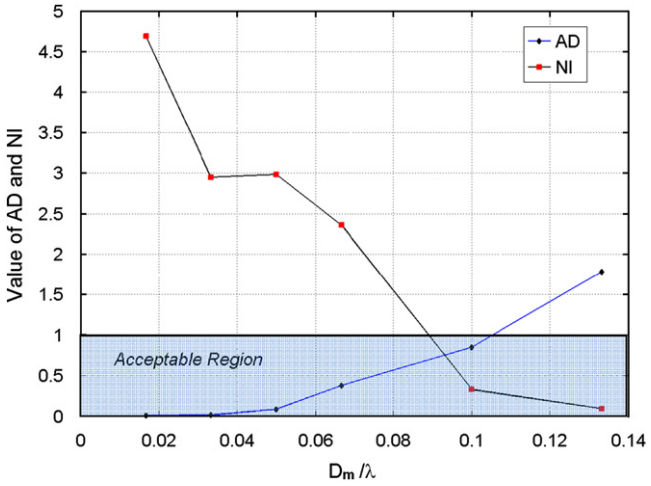

Fig. 9. Variation in AD and NI for the beam in Fig. 2 under different D_m/λ for cases in Fig. 7 ($\Xi_c=0.8$).

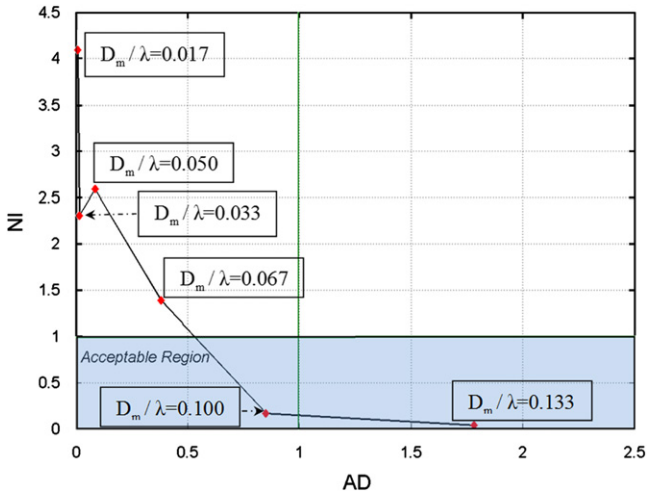

Fig. 10. Two-dimensional AD–NI presentation under different D_m/λ for cases in Fig. 7 ($\Xi_c=0.8$).

respectively, and Fig. 12 shows their corresponding two-dimensional AD–NI presentation with one more additional case ($d/\lambda=0.200$). It can be seen from both sets of figures that, regardless of damage length d, the optimal selection of $D_m/\lambda=0.1$ (*viz.*, roughly ten measurement points per wavelength) as suggested in Section 3.4.2 does not seem to be affected.

It is highly noteworthy that, with such an optimal selection, this approach is even able to detect damage which is much smaller than wavelength λ, showing advantages over conventional vibration-based detection (via which the minimum detectable damage is often over 10% of the overall size of the structure under inspection) and also outperforming elastic-wave-based damage detection (via which only when the damage is larger than half the wavelength can it be detected). Among six discussed cases in Fig. 11, the smallest detectable damage, without applying any signal de-noising processing, is only 3.3% of the wavelength (when $d/\lambda=0.033$).

Fig. 13 shows the two-dimensional AD–NI presentation at different degrees of stiffness reduction (SR=10%, 20%, 30%, 40%, 50%, 60%, respectively), to observe that the higher the SR, the more options are available for selecting D_m/λ with both acceptable AD and NI. Conclusively, under the given noise level (*i.e.*, 1% error in magnitude and 1° error in phase), the one of $D_m/\lambda=0.1$ (roughly ten measurement points per wavelength) is the most optimal selection for all the discussed cases, leading to a recommendable compromise between accuracy of finite difference and tolerance to measurement noise. Such a conclusion is also applicable to more severe noise contamination up to 10% error in magnitude or 5° error in phase as demonstrated by the authors elsewhere [29].

3.5. Data fusion for further improvement of precision

Reaching this stage, it is clear that this approach provides a flexible framework for practical implementation. DI_i can be constructed under different forcing frequencies and different measurement resolutions, with or without wavenumber filtering, *etc*. This makes it possible to generate a large quantity of DI_i plots or mappings. On the other hand, it is noticed that, during practical implementation, captured signals are prone to contamination from a variety of interference sources including measurement noise and uncertainties, boundary effects and error of finite difference, possibly dimming damage-related signal features and leading to inaccurate or even erroneous identification. Allowing for the above two aspects, a data fusion technique was included in this approach to combine damage indices constructed under different measurement configurations, with an aim of further improving the detection precision.

Data fusion herein can generally be understood as a technique appropriately aggregating two or more information sources obtained under different circumstances, to achieve a specific purpose such as enhanced signal-to-noise ratio or improved identification precision. In the approach, damage indices at individual measurement point i were obtained under K different measurement configurations, denoted by DI_{i-1},DI_{i-2},…,DI_L,…,DI_{i-K} ($L=1, 2, \ldots, K$), respectively, and all of them were subsequently amalgamated via a hybrid fusion scheme developed in authors' previous work [30,31], which is defined as

$$\mathrm{DI}_{i\text{-hybrid}} = \mathrm{DI}_{i\text{-geometric}} \cap \mathrm{DI}_{i\text{-arithematic}}, \tag{20}$$

where

$$\mathrm{DI}_{i\text{-geometric}} = \sqrt[K]{\mathrm{DI}_{i-1}\cdot \mathrm{DI}_{i-2}\cdots \mathrm{DI}_{i-L}\cdots \mathrm{DI}_{i-K}}, \quad \mathrm{DI}_{i\text{-arithematic}} = \frac{1}{K}\sum_{L=1}^{K} \mathrm{DI}_{i-L}. \tag{21}$$

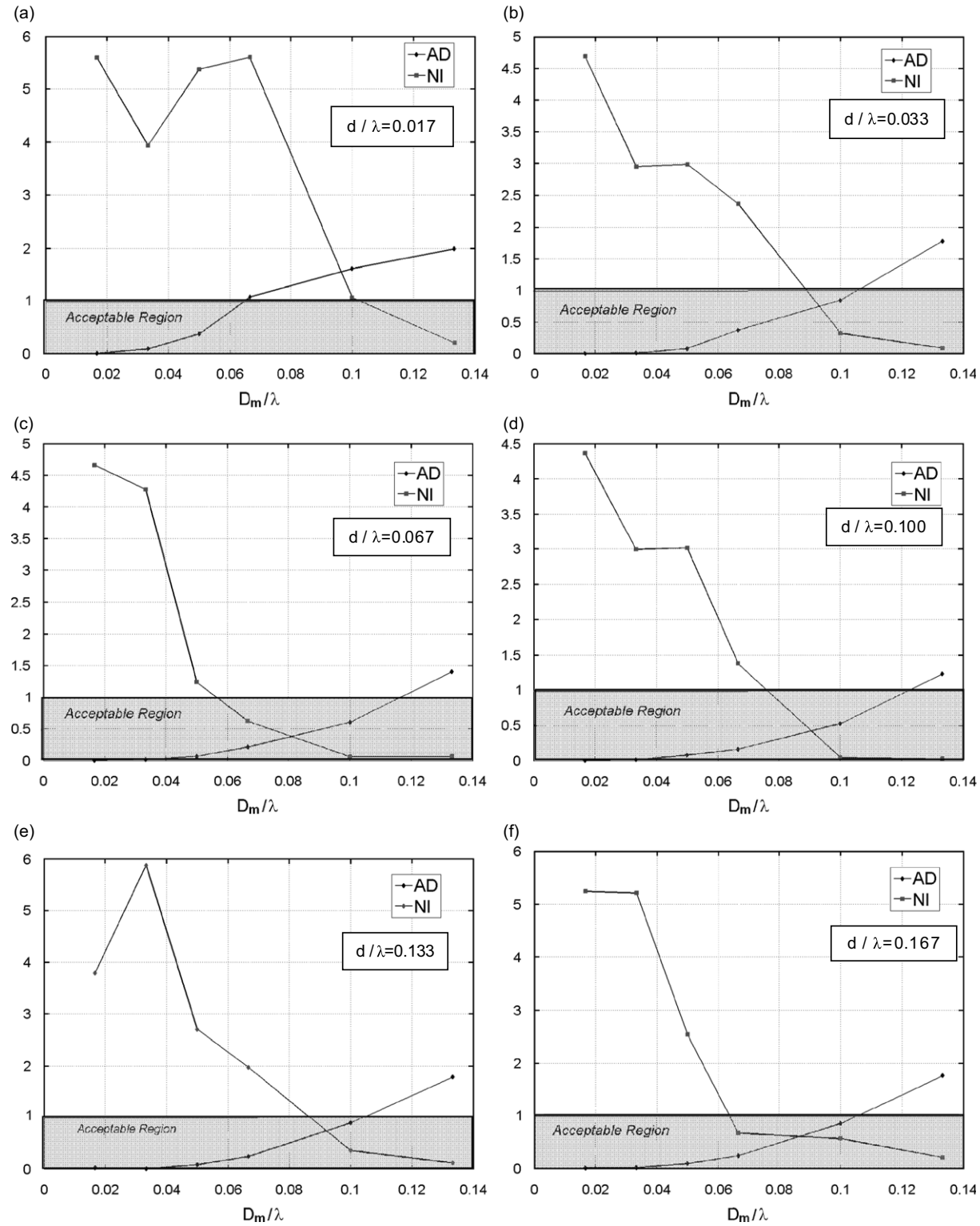

Fig. 11. Variation in AD and NI for the beam in Fig. 2 when d/λ is (a) 0.017; (b) 0.033; (c) 0.067; (d) 0.100, (e) 0.133; and (f) 0.167 (Ξ_c=0.8).

$DI_{i\text{-hybrid}}$ is the ultimate damage index at measurement point i upon data fusion. In such a hybrid fusion scheme, the arithmetic fusion ('$\sum$' in Eq. (21)) equally takes into account all prior perceptions pertaining to damage (DI_L, $L=1, 2, \ldots, K$) constructed under individual measurement configurations (*e.g.*, different forcing frequencies) and well de-centralizes their

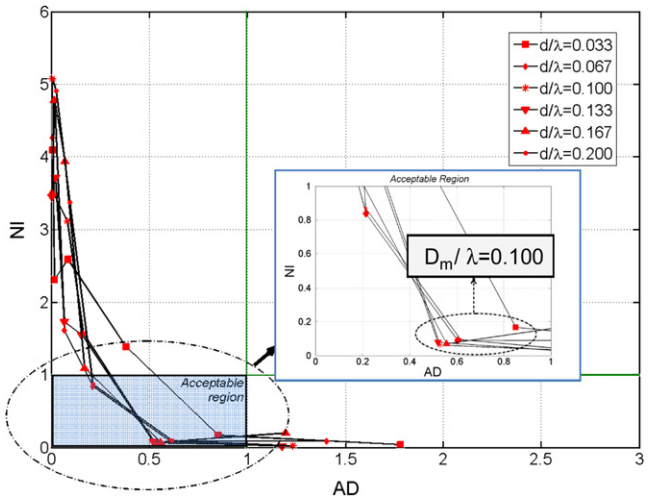

Fig. 12. Two-dimensional AD–NI presentation under different d/λ for cases in Fig. 11 (Ξ_c=0.8).

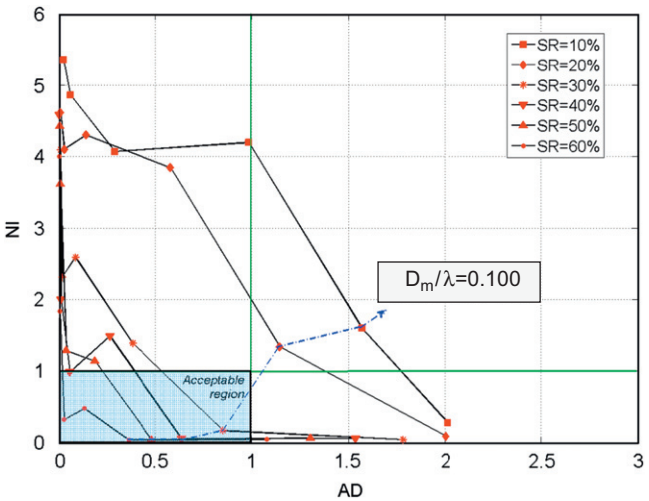

Fig. 13. Two-dimensional AD–NI presentation under different SR (d=20 mm and Ξ_c=0.8).

contributions in the ultimate damage index. However, although the arithmetic fusion guarantees a full inclusion of prior perceptions from all configurations, it is envisaged that information in all sources including ambient noise and measurement uncertainties are also included, which might 'pessimistically exaggerate' the possibility of damage presence, leading to a false alarm. To circumvent this problem, a geometric mean ('$\sqrt[K]{\ }$' in Eq. (21)) and further a conjunctive fusion ('$\cap$' in Eq. (20)) multiplicatively process individual source information. In this process, a low damage index at a measurement point under a particular measurement configuration leads to a significantly low likelihood of damage presence at that measurement point, showing good immunity to measurement noise and uncertainties. Through such a hybrid fusion, damage-related information (commonality in individual source information) is stood out and noise (random information in individual source information) is suppressed simultaneously. Effectiveness of the hybrid fusion defined by Eq. (20) will be demonstrated using experimental data in subsequent section.

4. Experimental validation

Albeit that the proposed methodology is not restricted by the complexity of the structure to be inspected, a simple cantilever beam was used in the experimental validation for easy understanding of principle of the approach. The beam can be a component of a complex system consisting of various structural components. This beam was made of aluminum alloy (360 mm long, 19 mm wide and 6 mm deep), with its material properties and geometric parameters tabulated in Table 1. A through-width notch (8 mm long and 2 mm deep) was machined, 260 mm away to the fixed beam end from its center (x_d=260 mm), as photographed in Fig. 14(a). An electro-mechanical shaker (B&K® 4809) was used to generate a harmonic excitation (f=140 Hz), applied 82 mm away from the fixed beam end (x_e=82 mm). The current selection of

Table 1
Material properties and geometric parameters of the beam used for experimental validation.

Density (kg/m^3)	2700
Young's Modulus E (GPa)	70
Beam length L (mm)	360
Width b (mm)	19
Thickness h (mm)	6
Location of excitation x_e (mm)	82
Length of inspection region $L_{\text{Inspection}}$ (mm)	240
Central location of damaged zone x_d (mm)	260
Length of damaged zone d (mm)	8

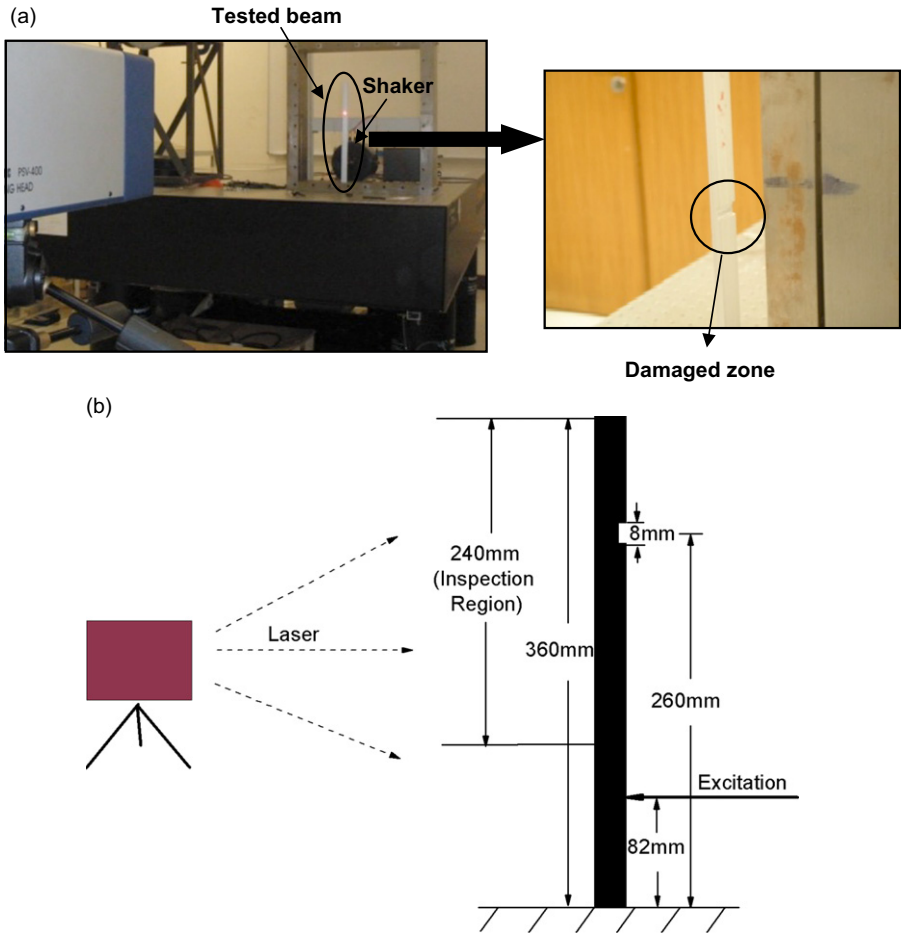

Fig. 14. Experimental setup for validation: (a) a through-width notch in the beam to be detected and (b) schematic of experimental setup.

excitation frequency was made in terms of experimentally obtained Frequency Response Function (FRF) curves, from which the resonance region was identified using the standard definition of the half-power bandwidth [32], to avoid the use of resonance frequency as explained in Section 2. Note that the use of a shaker was to simulate the vibration of the entire system under its normal operation. The excitation itself, however, was not directly used in data processing (to show that implementation of this approach is independent of external forcing frequency). Forty-nine measurement points were first selected and evenly distributed across the inspection region ($L_{\text{Inspection}}=240$ mm), and at this configuration the interval between two neighboring measurement points was 5 mm, leading to a high density configuration. The out-of-plane displacements were captured at each measurement point using a scanning Doppler laser vibrometer system (Polytec® PSV-400). Note that the displacements at measurement points were captured from the intact surface of the beam, opposite to which lay the damage, as shown schematically in Fig. 14(b).

Upon application of the rectangular window for eliminating the Gibbs phenomenon, the constructed DI_i curve across the inspection region using Eq. (11) is presented in Fig. 15(a), in which the damaged zone cannot be clearly

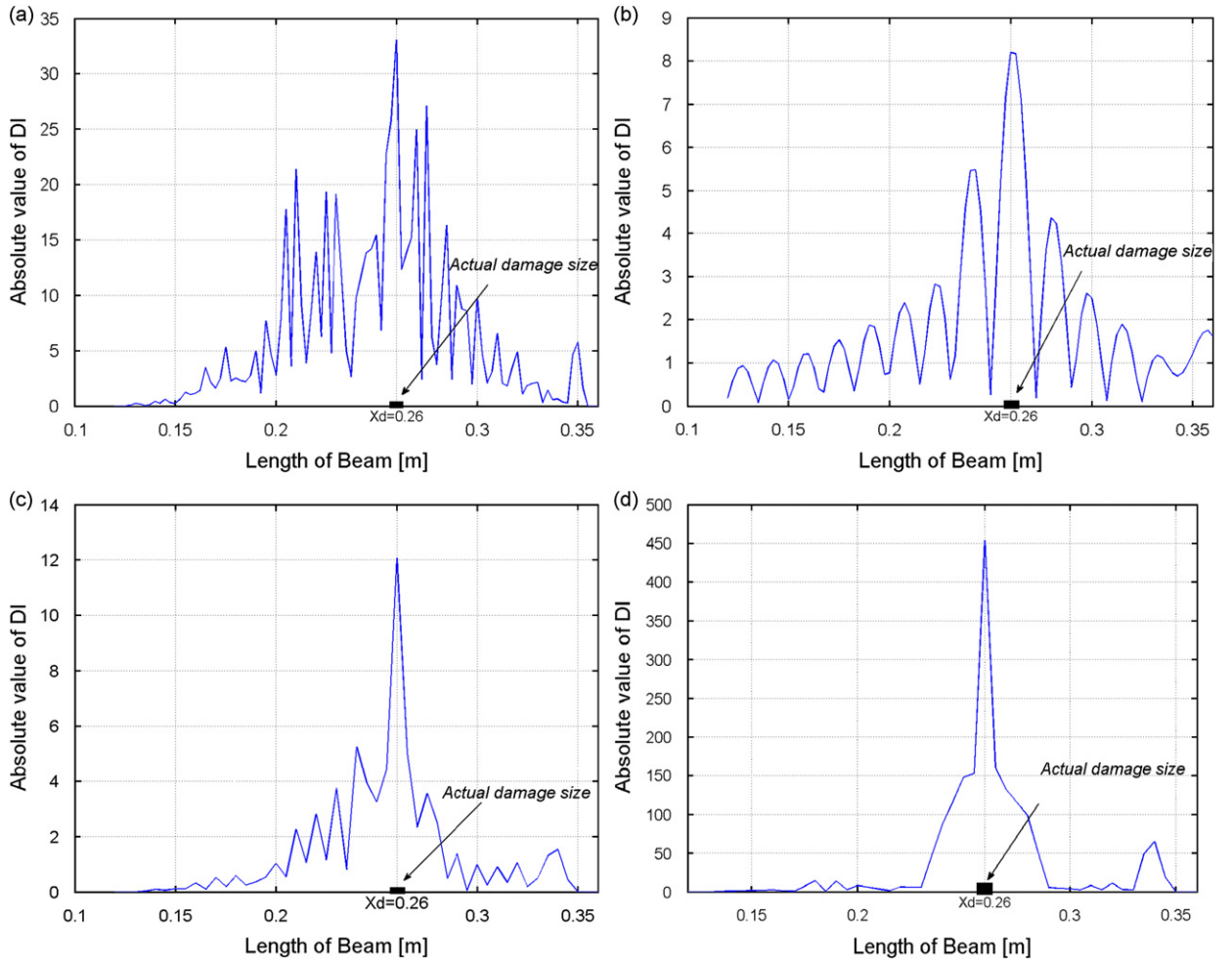

Fig. 15. Re-constructed DI_i at different measurement configurations: (a) $f=140$ Hz; number of measurement points: 49 (no wavenumber filtering applied); (b) $f=140$ Hz; number of measurement points: 49 (applied with developed low-pass wavenumber filter ($k_c=200$ rad/m)); (c) $f=140$ Hz; number of measurement points: 25 (no wavenumber filtering applied); and (d) $f=903$ Hz; number of measurement points: 25 (no wavenumber filtering applied).

identified without any de-noising processing. Treated with the low-pass wavenumber filtering ($k_c=200$ rad/m) developed in Section 3.3, the processed DI_i curve is shown in Fig. 15(b), from which both the presence and location of the damaged zone can be recognized roughly, demonstrating effectiveness of the low-pass wavenumber filtering in handling noise-polluted signals experimentally captured. In parallel with the use of the wavenumber filtering, by reducing the number of measurement points from 49 to 25 (but without applying the wavenumber filtering), Fig. 15(c) exhibits the accordingly obtained DI_i curve, in which DI_i in the damaged zone stood out prominently. This further supports the conclusion drawn in Section 3.4 that, with a proper choice of measurement parameters, the wavenumber filtering may not even be of necessity. Furthermore, Fig. 15(d) presents the DI_i curve after increasing the excitation frequency from $f=140$ Hz to $f=903$ Hz while remaining 25 measurement points and without applying the wavenumber filtering, to also observe improvement in detection accuracy, emphasizing the flexibility of the approach in implementation. Conclusively, during practical implementation, two de-noising techniques can be applied independently, rather than used either simultaneously or subsequently. In the current validation, with proper selection of a measurement configuration, acceptable identification results have been achieved even without the use of wavenumber filtering, as the results shown in Fig. 15(c) and (d).

Thanks to the diversity of de-noising treatments proposed in the study, only a few tests under different measurement configurations (*e.g.*, different densities of measurement points or different excitation frequencies) are sufficient to form a large data pool, from which various data sets (as individual source information) can be created for fusion. In an extreme case, if the structure is subject to a random excitation in a broadband frequency range, a single test would be enough because the information corresponding to different frequencies can be extracted from the measured FRF. To demonstrate this, the above three DI_i plots (Fig. 15(b)–(d)), obtained under different experiment configurations and applied with different signal processing, were fused using the hybrid data fusion scheme described by Eq. (20), to obtain the ultimate DI_i

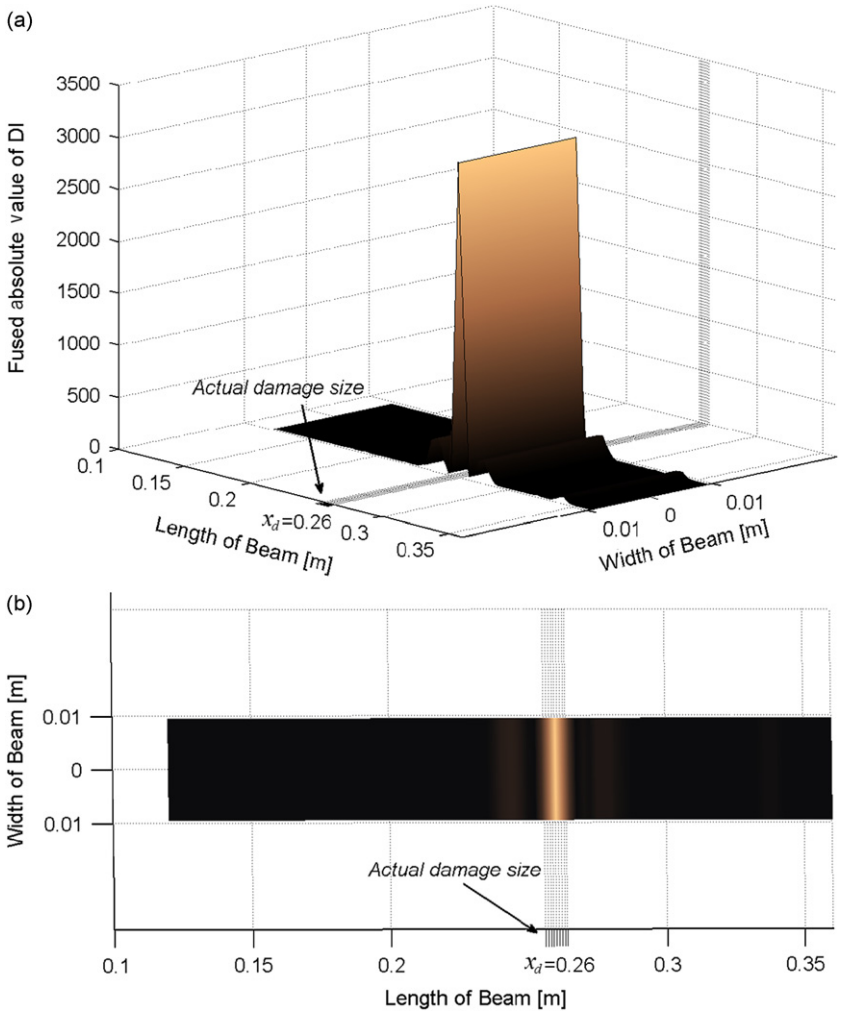

Fig. 16. (a) Fused ultimate DI_i plot using the plots in Fig. 15(b)–(d) and (b) two-dimensional view of (a) from the top.

curve, shown in Fig. 16. It is clear that the fused plot presents a much more explicit and intuitive indication of the presence and length of the damaged zone.

5. Conclusions

A novel damage identification approach based on local perturbation to dynamic equilibrium of the structural component under inspection was developed. Both simulation and experiment results have shown that the approach is able to bypass major limitations of conventional global vibration-based or local guided-wave-based damage detection philosophies, presenting a number of unique and appealing features: it requires neither benchmark structures nor baseline signals; neither global models nor prior knowledge on structural boundary conditions; plus no particular requirement for an additional excitation as long as the structure undergoes steady vibration during its normal operation. In addition, benefiting from its local inspection nature, the approach can be readily extended to the detection of multiple-damage within the same inspection region, showing advantages over conventional global detection.

However, limitations of the approach should be envisaged. Under some circumstances, it may be a challenging task to achieve the local equilibrium relationship for a complex structural component (*e.g.*, composite materials), although local FE model can be created to facilitate the obtainment of such a relationship. Moreover, as observed, the influence of measurement noise can jeopardize detection accuracy and precision seriously, making a de-noising treatment indispensable in some practical applications. Towards this limitation, alternatives were provided in this study: (i) application of low-pass filtering in a wavenumber domain to screen out high-wavenumber noise contamination; and (ii) proper selection of measurement configurations. For the latter, the spatial resolution for displacement measurement is shown to be vital in balancing detection accuracy and noise immunity of the method. An optimal selection of D_m/λ is dependent on the noise level. A lower measurement noise level allows lower D_m/λ, so that more measurement point can be used to enhance the

identification accuracy. As an example, when measurement noise is around 1% in amplitude and 1° in phase, as a rule of thumb, a selection of ten measurement points per wavelength seems to be a practical and optimal criterion to warrant acceptable accuracy, even without application of any de-noising treatment. As a last resort, a data fusion scheme can be applied to further enhance the detection capability. Effectiveness of the approach was experimentally examined by quantifying damage in a beam using a scanning laser vibrometer. As a final note, it should be mentioned that this proposed methodology is applicable to complex systems comprising various structural components, provided that the local equilibrium relationship of a component of interest is known *a priori*.

Acknowledgments

L. Cheng and Z. Su wish to acknowledge the support given to them by the Hong Kong Polytechnic University (Research Grants G-U859 and A-PE1F).

References

[1] G.R. Tillack, J. Gray, X-ray imaging methods over the last 25 years—new advances and capabilities, D.O. Thompson, D.E. Chimenti (Eds.), *Review of Progress in Quantitative Nondestructive Evaluation*, Vol. 20, American Institute of Physics, New York, 2001, pp. 16–32.
[2] J.D. Achenbach, Quantitative nondestructive evaluation, *International Journal of Solids and Structures* 37 (2000) 13–27.
[3] H. Sohn, C.R. Farrar, F.M. Hemez, D.D. Shunk, D.W. Stinemates, B.R. Nadler, J.J. Czarnecki, A Review of Structural Health Monitoring Literature: 1996–2001, Los Alamos National Laboratory Report, LA-13976-MS, 2003.
[4] C. Boller, Ways and options for aircraft structural health management, *Smart Materials and Structures* 10 (2001) 432–440.
[5] F.-K. Chang, Introduction to health monitoring: context, problems and solutions. *Presentation at the First European Pre-workshop on Structural Health Monitoring*, Paris, France, July, 2002.
[6] S.W. Doebling, C.R. Farrar, M.B. Prime, D.W. Shevitz, Damage Identification and Health Monitoring of Structural and Mechanical Systems from Changes in their Vibration Characteristics: A Literature Review, Los Alamos National Laboratory Report, LA-13070-MS, 1996.
[7] J.L. Rose, *Ultrasonic Waves in Solid Media*, Cambridge University Press, New York, 1999.
[8] W. Fan, P. Qiao, Vibration-based damage identification methods: a review and comparative study, *Structural Health Monitoring: An International Journal* 10 (2011) 83–111.
[9] Y.S. Lee, M.J. Chung, A study on crack detection using eigenfrequency test data, *Computers and Structures* 77 (2000) 327–342.
[10] J.T. Kim, Y.S. Ryu, H.M. Cho, N. Stubbs, Damage identification in beam-type structures: frequency-based method vs. mode-shape-based method, *Engineering Structures* 25 (2003) 57–67.
[11] A.K. Pandey, M. Biswas, M.M. Samman, Damage detection from changes in curvature mode shapes, *Journal of Sound and Vibration* 145 (2) (1991) 321–332.
[12] V. Giurgiutiu, C.A. Rogers, Recent advancements in the electro-mechanical (E/M) impedance method for structural health monitoring and NDE, *Proceedings of SPIE on Smart Structures and Materials*, Vol. 3329, 1998, pp. 536–547.
[13] A.K. Pandey, M. Biswas, Damage detection in structures using changes in flexibility, *Journal of Sound and Vibration* 169 (1) (1994) 3–17.
[14] Y. Aoki, O. Byon (Goichi Ben), Damage detection of CFRP pipes and shells by using localized flexibility method, *Advanced Composite Materials* 10 (2001) 189–198.
[15] A.M. Yan, J.C. Golinval, Structural damage localization by combining flexibility and stiffness methods, *Engineering Structures* 27 (2005) 1752–1761.
[16] G. Kawiecki, Modal damping measurement for damage detection, *Smart Materials and Structures* 10 (2001) 466–471.
[17] Z. Su, L. Ye, Y. Lu, Guided Lamb waves for identification of damage in composite structures: a review, *Journal of Sound and Vibration* 295 (2006) 753–780.
[18] W. Ostachowicz, P. Kudela, P. Malinowski, T. Wandowski, Damage localisation in plate-like structures based on PZT sensors, *Mechanical Systems and Signal Processing* 23 (2009) 1805–1829.
[19] P. Fromme, P.D. Wilcox, M.J.S. Lowe, P. Cawley, On the development and testing of a guided ultrasonic wave array for structural integrity monitoring, *IEEE Transactions on Ultrasonics Ferroelectrics and Frequency Control* 53 (2006) 777–785.
[20] A. Raghavan, C.E.S. Cesnik, Review of guided-wave structural health monitoring, *The Shock and Vibration Digest* 39 (2007) 91–114.
[21] L. Wang, F.G. Yuan, Damage identification in a composite plate using prestack reverse-time migration technique, *Structural Health Monitoring: An International Journal* 4 (2005) 195–211.
[22] J.-B. Ihn, F.-K. Chang, Pitch-catch active sensing methods in structural health monitoring for aircraft structures, *Structural Health Monitoring: An International Journal* 7 (2008) 5–19.
[23] J.E. Michaels, T.E. Michaels, Guided wave signal processing and image fusion for in situ damage localization in plates, *Wave Motion* 44 (2007) 482–492.
[24] X. Zhao, H. Gao, G. Zhang, B. Ayhan, F. Yan, C. Kwan, J.L. Rose, Active health monitoring of an aircraft wing with embedded piezoelectric sensor/actuator network: I, defect detection, localization and growth monitoring, *Smart Materials and Structures* 16 (2007) 1208–1217.
[25] C.R. Farrar, D.A. Nix, W. Scott, S.W. Doebling, Vibration-based structural damage identification, *Philosophical Transactions of the Royal Society of London Series A* 359 (2001) 131–149.
[26] K. Worden, C.R. Farrar, G. Manson, G. Park, The fundamental axioms of structural health monitoring, *Proceedings of the Royal Society A* 463 (2007) 1639–1664.
[27] C. Pezerat, J.L. Guyader, Two inverse methods for localization of external sources exciting a beam, *Acta Acustica* 3 (1995) 1–10.
[28] C. Pezerat, J.L. Guyader, Force analysis technique: reconstruction of force distribution on plates, *Acta Acustica United with Acustica* 86 (2000) 322–332.
[29] H. Xu, L. Cheng, Z. Su, J.L. Guyader, Characterizing structural damage based on locally perturbed dynamic equilibrium, *Proceedings of the Eighth International Workshop on Structural Health Monitoring*, Stanford, CA, USA., September 2011.
[30] Z. Su, X. Wang, L. Cheng, L. Yu, Z. Chen, On selection of data fusion schemes for structural damage evaluation, *Structural Health Monitoring: An International Journal* 8 (2009) 223–241.
[31] Z. Su, L. Cheng, X. Wang, L. Yu, C. Zhou, Predicting delamination of composite laminates using imaging approach, *Smart Materials and Structures* 18 (7) (2009) 074002 (8 pp).
[32] J. He, Z.F. Fu, *Modal Analysis*, Butterworth-Heinemann, Oxford, 2001.